# Combination of EPR Measurements and DFT Calculations To Study Nitrate Impurities in the Carbonated Nanohydroxyapatite

Timur Biktagirov,[†] Marat Gafurov,[*,†] Georgy Mamin,[†] Elena Klimashina,[‡] Valery Putlayev,[‡] and Sergei Orlinskii[†]

[†]Institute of Physics, Kazan Federal University, Kremlevskaya Street 18, 420008 Kazan, Russian Federation
[‡]Faculty of Materials Science, Moscow State University, Leninskie Gory, 119991 Moscow, Russian Federation

ABSTRACT: We demonstrate the application of the combined experimental–computational approach for studying the anionic impurities in hydroxyapatite (HAp). Influence of the carbonation level (x) on the concentration of the NO_3^{2-} radicals in the HAp nanocrystals of $Ca_{10-x}Na_x(PO_4)_{6-x}(CO_3)_x(OH)_2$ with x in the range $0 < x < 2$ and average sizes of 30 nm is investigated by different analytical methods including electron paramagnetic resonance (EPR). Stable NO_3^{2-} radicals are formed under X-ray irradiation of nano-HAp samples from NO_3^- ions incorporated in trace amounts during the wet synthesis process. Density functional theory (DFT) based calculations show energetic preference for the PO_4 group substitution by NO_3^- ions. Comparison of the calculated and experimental spectroscopic parameters (g and hyperfine tensors) reveals that EPR detects the NO_3^{2-} radicals located in the positions of the PO_4 group only. It is shown that with the increase in x, the carbonate ions substitute the NO_3^{2-}/NO_3^- ions. DFT calculations confirm that carbonate incorporation in HAp structure is energetically more favorable than the formation of the nitrate defect.
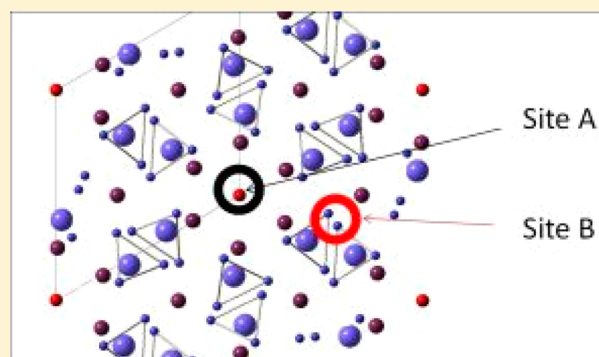
1. INTRODUCTION

Hydroxyapatite ($Ca_{10}(PO_4)_6(OH)_2$, HAp) is one of the basic materials used in bone implant surgery. Because of such features as high biocompatibility, osteoconductivity, very good adaptation under in vivo conditions, and chemical composition mirroring that of bone mineral and teeth enamel, it is widely applied to fill bone defects in orthopedics, maxillofacial surgery, and stomatology.[1−3] It is thought that HAp nanoparticles (nano-HAp) are better candidates for an apatite substitute of bone in biomedical applications than microsized hydroxyapatite (micro-HAp).[4−6] Nano-HAp has the potential to improve current disease diagnosis due to its ability to circulate in the blood and to deliver and to distribute a payload to image tissues and cells in the body for bioimaging and therapeutical applications.[7,8] Antitumor (inhibitory) action of nano-HAp is reported.[9] High sorption activity to a number of various anions and cations including those of some heavy metals and radionuclides makes the nano-HAp based substances important not only in the biomedical area but also for waste management and in catalysts production.[10,11]

Synthetic HAp presents a good implant only if it is modified by other ions. Carbonate ion is prevailed among others (in the HAp of biogenic origin its concentration can amount to 8 wt %) but by far not a solitary one.[12,13] The mutual influence of different ions and complexes by simultaneous substitution/ incorporation on the properties of the HAp and their competition for the positions in the HAp structure (especially in the case of the nanosized materials) is of a great interest over the past few years.[14,15]

There is a long-standing controversy concerning the relationship between a few percent carbonate and its location in the lattice structure of apatite (see refs 16 and 17 for the recent literature reviews on this issue). It is generally accepted that the principal possible sites for CO_3^{2-} ions in HAp are either on the site substituting for OH^- ions or on a site substituting for PO_4^{3-} ions, named, respectively type A and type B substitutions. It seems to be that depending on the preparation procedure or type of the natural HAp, carbonate could be found in these two different locations (or distributed between them). Because of the complicated structure and large unit cell size (44 atoms per unit cell for the hexagonal structure or even 88 atoms in the case of the monoclinic configuration), it is only recently that HAP has begun being studied using semiempirical and first-principles calculation methods.[17,18] Though all the applied simulation methods are promising, there remain apparent discrepancies and contradictions between them and experimental results (see refs 17, 19, and 20 for examples). Further experimental efforts, verification, and refinements of the models applied could be done especially in the case of nanomaterials whose properties depend on the synthesis route and conditions to a greater degree.
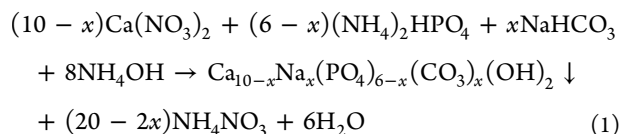
Among the diversity of methods for synthesizing the modified HAp powders, the wet (precipitation) chemical procedure involving the aqueous solutions of the nitrogen-containing compounds is the one most commonly used.[12,21] In a series of papers[22−27] it was shown by electron paramagnetic resonance (EPR) methods that the nitrogen-containing species could be incorporated into the apatite-like structures. This might change a biocompatibility of the HAp-based materials.[28] Application of HAp as a highly efficient absorber of nitrates for the soil and groundwater remediation was demonstrated in ref 29. Identification of the nitrogen-containing species in trace amounts by standard laboratory analytical tools and elimination of those from the synthesized materials are quite complicated tasks. To make the nitrates detectable by EPR, HAp samples are exposed to X-rays, γ-rays, or ultraviolet or other types of ionizing radiation. The most stable nitrogen-containing radical formed in this way is NO_3^{2-}.

Conventional continuous wave (CW) EPR is widely used for the detection of various types of radiation defects (which are usually ascribed to the different carbonate, phosphorus, hydroxyl, and oxygen radicals), for the detection of paramagnetic impurities such as lanthanides or Mn^{2+} sorbed on HAp or embedded into the lattice, for the determination of their structure and localization, and for qualitative and quantitative analyses, etc. (see ref 16 for one of the recent reviews). However, EPR is still not considered as a standard tool for the comprehensive characterization of the HAp-based materials.[30]

In this work a series of HAp samples with the different carbonation level x prepared by the wet technique is investigated chemically by X-ray diffraction (XRD), electron microscopy combined with the energy dispersive spectroscopy (EDS), Fourier-transformed infrared (FTIR), and EPR methods. The influence of the carbonation degree on the amount of the NO_3^{2-} radicals is detected and examined by EPR methods before and after X-ray irradiation of the samples. Possible origins of such changes are discussed. Ab initio density functional theory (DFT) based calculations are performed in order to establish the energetically preferable configuration for NO_3^{-}/NO_3^{2-} substituted HAp. Spectroscopic parameters (components of g-factor and hyperfine interaction tensor $\mathbf{A}$) for NO_3^{2-} are computed.

2. MATERIALS AND METHODS

Syntheses of the nano-HAp samples and carbonated nano-HAp samples are described in refs 19 and 31 in detail. Briefly, nanopowders of the carbonated HAp with various degrees of carbonate substitution were prepared by the aqueous precipitation method according to the following equation:

$$(10 - x)Ca(NO_3)_2 + (6 - x)(NH_4)_2HPO_4 + xNaHCO_3$$
$$+ 8NH_4OH \rightarrow Ca_{10-x}Na_x(PO_4)_{6-x}(CO_3)_x(OH)_2 \downarrow$$
$$+ (20 - 2x)NH_4NO_3 + 6H_2O \qquad (1)$$

where x = 0, 0.25, 0.5, 0.75, 1, 1.5, 2 by dropwise addition of 0.3 M stock solution of $(NH_4)_2HPO_4$ (99.9%, Labteh, Russia) with appropriate amount of $NaHCO_3$ (99.9%, Labteh, Russia) to 0.5 M stock solution of $Ca(NO_3)_2 \cdot 4H_2O$ (99.9%, Labteh, Russia). Sodium carbonate was introduced as a source of Na to compensate the charge imbalance caused by CO_3^{2-} substitution. Prior to preparation of the stock solutions, all the reagents were checked for the content of main substances by

gravimetric or titrimetric chemical analyses. The pH value of the stock solutions was preadjusted at 11.5 by addition of NH_4OH, and then it was maintained manually at the constant value of 12.0(5) by addition of the concentrated solution of ammonium hydroxide. The temperature was controlled and stabilized at 80(1) °C. After total mixing of the stock solutions, the suspension was ripened and heated using a thermostatically controlled hot plate for 24 h to reach roughly 30 nm crystallites under constant stirring. Then the precipitate was filtered and thoroughly washed with 300 mL of distilled water. The resulting precipitate was dried at room temperature in air. Dry powders were heat-treated for 1 h at 260 °C in air and annealed to 400 °C for 4 h under vacuum ($<10^{-4}$ mbar) in order to reach better crystallinity and to eliminate the adsorbed moisture and synthesis residues such as nitrous species. It was concluded that this thermal treatment did not affect the structure of the precipitates, since the lattice parameters changed slightly (less than 0.0005 nm), there were no differences in FTIR spectra, and Ca/P ratio remained unchanged.

The main advantages of the aqueous precipitation process are the following: (i) high yield of targeted phase of nano-HAp in one run due to significant solubility of calcium nitrate in water; (ii) fast production rate; (iii) low processing costs; (iv) the only byproduct consists of ammonium nitrate irreversibly decomposed at temperatures higher than 210 °C into two or three gases—water vapor and nitrogen oxide (I), N_2O (below 270 °C), or water vapor nitrogen and oxygen (>270 °C) (i.e., it is possible, in principle, to obtain HAp of the highest purity after calcination of the precipitate); (v) the material can be easily modified by different dopants. However, in the case of using the HAp precipitate, (i) one has to spend time on washing the precipitate to remove nitrate residues and (ii) the resulting product can be greatly affected by even a slight difference in the reaction conditions.

The powders were studied by XRD analysis in the interval of angles 2Θ = (10−110)° (Cu Kα radiation, Rigaku D/MAX 2500 with rotating anode) and FTIR spectroscopy in the 400−4000 cm^{-1} range (Perkin-Elmer 1600). Average sizes of crystallites were extracted from the XRD line profile (002) using Scherrer and Wilson formulas from Williamson−Hall plots according to the procedure described in ref 32. The lattice parameters were estimated using WinX^{POW} powder diffraction software. The micromorphology of the powders was examined by scanning and transmission electron microscopy (SEM/TEM) (JEM-2000FX II, JEOL, operated at 200 kV, and FESEM LEO SUPRA 50VP, Carl Zeiss, 5 kV). The Ca and P contents of the powders were estimated by EDS (INCA Energy +, Oxford Instruments, attached to LEO SUPRA 50 VP).

X-ray irradiation of the synthesized nanopowders was performed using a URS-55 tube (U = 55 kV, I = 16 mA; W, anticathode) at room temperature (RT) with an estimated dose of 5 and 10 kGy to create stable paramagnetic centers. XRD patterns before and after X-ray irradiation were checked by a D2 Phaser diffractometer, Bruker.

Pulsed and continuous wave EPR measurements were done using X-band (9 GHz) Bruker Elexsys 580 spectrometer. EPR spectra were recorded by means of the conventional continuous wave modulation technique as well as by the field-swept two-pulse echo sequence (FS-ESE) $\pi/2-\tau-\pi$ with the length of the π pulse of 16 ns and time delay τ = 200 ns.

DFT based calculations have been carried out within the framework of the plane-wave pseudopotential approach implemented in the open-source Quantum ESPRESSO pack-

age.[33] Perdew–Burke–Ernzerhof version of the generalized gradient approximation of the exchange-correlation functional (GGA-PBE)[34] and the Vanderbilt ultrasoft pseudopotentials[35] were employed. Extensive convergence tests have defined energy cutoffs of 40 Ry for the smooth part of the electron wave functions and 320 Ry for the augmented electron density. The results presented here were obtained for a $1 \times 1 \times 1$ monoclinic supercell (space group $P2_1/b$, 88 atoms in case of pure HAp; simulation of HAp is usually not performed within $P6_{3/m}$ space group because of the unphysical duplication of each OH group by the m-mirror). The difference in the notations of principal axes for the hexagonal and monoclinic modifications should not lead to confusion. The test calculations with the larger structures ($1 \times 2 \times 1$ monoclinic cell) revealed no appreciable differences in the computed properties, confirming the convergence of the supercell size. Unit-cell and initial positional parameters for HAp were taken from ref 36. During geometry optimization, the cell dimensions and atomic positions were allowed to be fully relaxed with the convergence condition on forces of 10^{-3} au. The Brillouin Zone integration was restricted to Γ-point during structural optimization, whereas the Monkhorst–Pack scheme[37] with appropriate k-point meshes was used for the calculation of the total energies. Spectroscopic parameters (constants of the hyperfine interaction $\mathbf{A}$ of the unpaired electron with ^{14}N nucleus and $\mathbf{g}$ tensors) for the nitrogen-containing radicals were extracted by using the gauge-including projector augmented wave (GIPAW) approach.[38] The standard Troullier–Martins norm-conserving pseudopotentials[39] with GIPAW projectors were used. Converged results were obtained with a plane-wave energy cutoff of 70 Ry. We have also carefully ensured the convergence of the calculated $\mathbf{g}$-tensor with respect to the number of k-points (the computation of $\mathbf{g}$-tensor requires denser k-point grid compared to that needed for hyperfine tensor); the reciprocal spacing of about 0.35 nm^{-1} in each lattice direction was found to be sufficient. For the simulation of EPR spectra EasySpin toolbox for MatLab[40] was exploited. The values of A and g obtained using GIPAW were used for the EPR spectrum simulation in tensor form explicitly.

We have also performed DFT calculations for the isolated free radical NO_3^{2-} with B3LYP/EPR-II implemented in ORCA program system[41] to compare with the results obtained for those in the HAp crystal.

3. RESULTS AND DISCUSSION

3.1. Experimental Results. XRD analysis shows that all the samples contain only one phase that can be treated as belonging to the $P6_{3/m}$ space group with the parameters of the unit cell close to $a' \approx b' \approx 0.9402(2)$ nm and $c' \approx 0.6890(2)$ nm for $x = 0$. (Considering the monoclinic symmetry $P2_1/b$ we used for DFT calculations, one can write the lattice parameters as $a \approx 0.940$ nm, $b \approx 0.689$ nm, and $c \approx 1.88$ nm.) A noticeable reduction of the cell volume of about 1.2% was obtained in the microcrystalline HAp with the carbonate concentration increase in the range $0.5 < x < 1.5$.[31]

Corresponding EDX measurements ensured the ratio close to Ca/P = 1.70(3) was within the accuracy of our experiments for the samples with $x = 0$ serving as evidence of the stoichiometry of the synthesized HAp species. The obtained ratio suggested that a part of phosphates is substituted (presumably by carbonates). The results of the volumetric measurements to define the real carbonate concentration are presented in Figure 1.
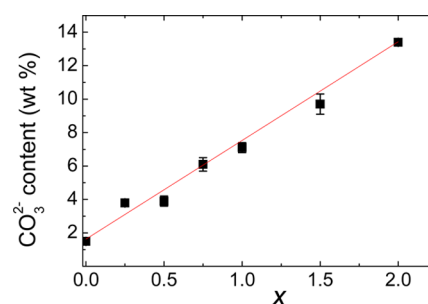

Figure 1. Measured by the volumetry CO_3^{2-} content in wt % as a function of carbonation level x along with the corresponding linear approximation. The values were approximated by the linear equation content(CO_3^{2-}) = 1.6(3) + 5.9(2)x as shown by the red solid line.

Corresponding FTIR measurements also show that even in the sample with $x = 0$ the carbonates' vibrations in the vicinities of 850–890 cm^{-1} (ν_2 mode) and 1400–1650 cm^{-1} (ν_3 mode) are present.[31,42] Their intensities are growing with x. No nitrate bands in the vicinities of 825 and 1385 cm^{-1} [42] in FTIR patterns were recorded. The only signal in the vicinity of 1385 cm^{-1} was registered in the carbonated HAp powder with $x = 1$ that was not washed after synthesis. No traces of the nitrogen containing impurities were found by EDS.

The synthesized HAp powders at RT are EPR silent. To create stable paramagnetic centers, the samples were irradiated by X-ray at RT. XRD patterns before and after X-ray irradiation are practically the same while EPR spectrum appears.

The EPR spectrum of X-ray irradiated HAp with $x = 0$ recorded in CW- and FS-ESE modes at RT is presented in Figure 2. The observed three-line pattern is due to the hyperfine interaction between the electronic spin with $S = \frac{1}{2}$ and one nuclear spin with $I = 1$ as the case for ^{14}N. The EPR spectrum obtained was ascribed to the stable NO_3^{2-} radicals in HAp.[22–27]

After X-ray irradiation at RT with the doses of about 5 and 10 kGy the intensity of the EPR signal does not change. Induced radicals' concentration of $4(1) \times 10^{18}$ spins per gram was estimated from a comparison of the integrated intensity of the spectra with that from the reference (Mn^{2+} in MgO crystal) in the sample of HAp with $x = 0$. It means that probably all the species responsible for the EPR spectrum are ionized even at 5 kGy and no additional NO_3^{2-} radicals could be created even at higher X-ray doses at RT. We did not investigate the concentration dependence for other irradiation doses and at lower temperatures.

These radicals formed this way are very stable. Under the storage at RT in a laboratory cupboard their concentration has reduced to half its initial value after 2 years. The attempts to remove them by heating or annealing at up to 400 °C during 4 h under 10^{-4} mbar vacuum did not reveal any changes in the intensity of the EPR spectrum.

Carbonation changes the obtained EPR spectrum. Figures 3 and 4 demonstrate this fact. At $x < 0.5$ the EPR spectra are dominated by the nitrate pattern, while at higher values of x the spectrum resembles that for the carbonate ions, CO_2^-. (Mammoth tusk dated 8–10 thousand years B.C. from the private collection of Prof. N. I. Silkin from the river Kama, Volga river region area, land Tatarstan, Russia, is employed as a reference for the "natural" hydroxyapatite. The most intensive EPR signal obtained after X-ray irradiation of that belongs to the CO_2^- radical[43]). These changes can be easily tracked on the
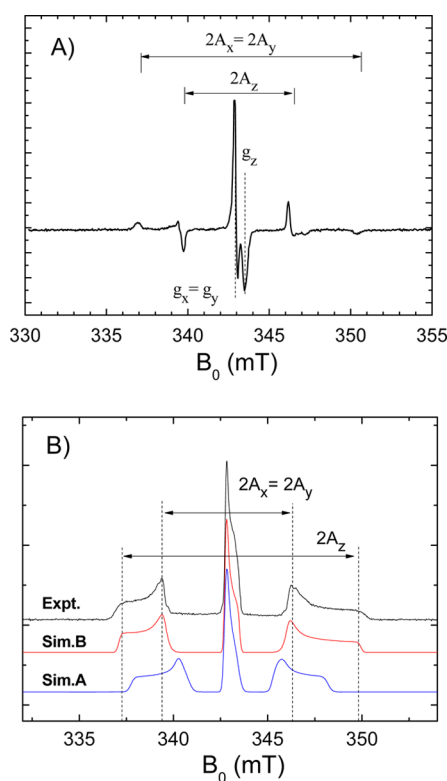
Figure 2. EPR spectrum caused by the presence of NO_3^{2-} in a powder of HAp with $x = 0$ after X-ray irradiation detected in (A) CW mode and (B) FS-ESE mode. The experimental FS-EPR spectrum (denoted as Expt.) in (B) is presented together with its simulation using the spectroscopic parameters obtained by GIPAW DFT calculations for B-type (Sim.B) and A-type (Sim.A) models (see section 3.2 for details). Components of $\mathbf{g}$ and $\mathbf{A}$ tensors are marked ($g_z = 2.0015(5)$, $g_x = g_x = 2.0055(5)$, $A_z = 6.65(40)$ mT, $A_x = A_y = 3.35(40)$ mT). Spectrum in CW mode (A) is registered by applying a microwave power of 20 μW and modulation amplitude of 0.1 mT.
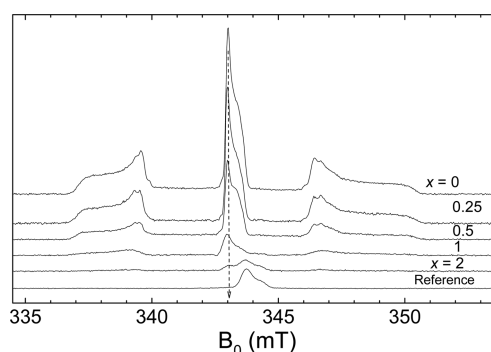

Figure 3. Evolution of the FS-ESE acquired EPR spectrum of NO_3^{2-} at RT with x. X-ray irradiated mammoth tusk serves as a reference for the "natural" hydroxyapatite carbonate containing radical. The vertical dashed arrow is a guide for the eye.

spectra acquired by FS-ESE (Figure 3). Because the longitudinal (T_1) and the transverse (T_2) electronic relaxation times for the NO_3^{2-} radicals are measured to be the same in the samples with $x = 0$, 0.5, and 1 (their exact values at a certain temperature are not important for this work and therefore are not presented), one could also use the intensities of the FS-ESE acquired EPR spectra for quantitative analysis (Figure 4).
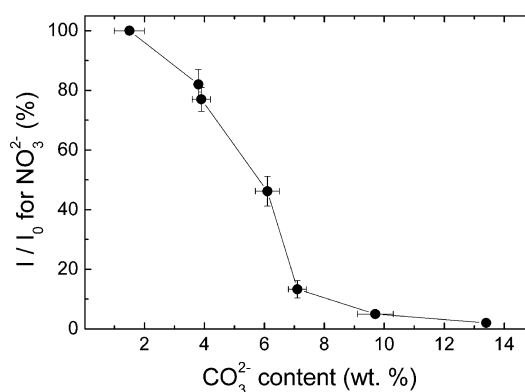

Figure 4. Dependence of the relative integrated intensity (I/I_0) of the EPR spectrum of NO_3^{2-} on carbonate concentration as taken from the volumetric analysis (Figure 1). The solid line is a guide for the eye.

3.2. DFT Calculations. Since NO_3^- (as a precursor for NO_3^{2-}) and CO_3^{2-} are isoelectronic ions with the same symmetry of ground sate (D_{3h}) and close ionic radii, it is logical to assume that NO_3^- occupies the same sites that the carbonate does. We have considered these two possible locations of NO_3^- ion in the HAp lattice. As is often presumed for the carbonate-doped HAp, we suggest that the charge compensation scheme for the B-type substitution is manifested in the removal of one of the nearest Ca.[42,44] We have performed full geometry optimization runs with different initial configurations. Figure 5b,c presents the most energetically favored structures. For both of the substitution models the nitrate ions have similar planar configuration with the average N–O distance of about 0.126 nm. It correlates with the 0.128 nm reported for CO_3^{2-}.[45,46] For the A-type substitution, the NO_3^- plane is
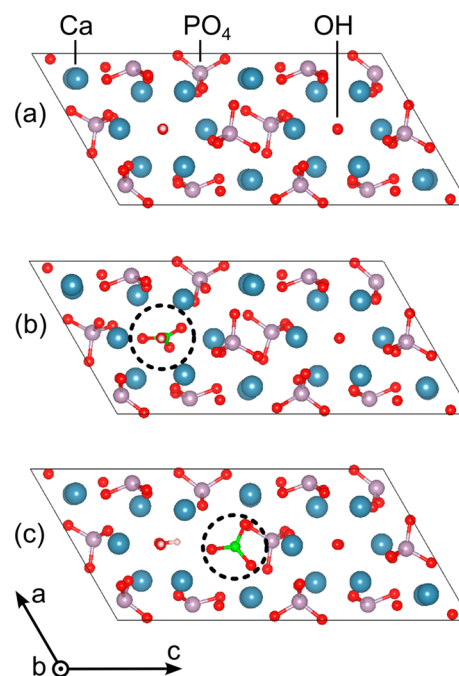

Figure 5. Optimized HAp structures for NO_3^- ions as seen in ac-plane: (a) pure HAp; (b) NO_3^- located in OH channel (A-site); (c) NO_3^- in the position of PO_4 (B-site). Ca, P, O, H, and N atoms are displayed as blue, purple, red, white, and green spheres, respectively. Positions of NO_3^- ions are marked by dashed-line circles.

tilted with respect to crystallographic *b*-axis, making an angle of about 153°. For the position in the PO_4 site the nitrate ion is almost perpendicular to the *b*-axis (the tilt angle is 79°).

As expected, the incorporation of NO_3^- causes some structural deformations of HAp lattice. However, the computed lattice parameters for both of the simulated models are still very close to those of pure HAp as shown in Table 1. It is in the range of 2% accuracy with the experimental values extracted by XRD measurements of our samples.

Table 1. Comparison between the Computed and Experimental Lattice Parameters (nm) and Cell Volumes (V, nm^3)

	a	*b*	*c*	*V*
DFT A-type substitution	0.957	0.689	1.922	1.098
DFT B-type substitution	0.947	0.690	1.903	1.071
DFT pure HAp	0.949	0.691	1.896	1.075
experiment[a]	0.940	0.689	1.880	1.055

[a]XRD data from this work for the sample with *x* = 0; for the sake of convenience, the principal axes were denoted as for monoclinic configuration.

The changes in the HAp lattice parameters with the incorporation of NO_3^- can be commented as follows. One could expect the increase in the lattice parameters for the A-type supercell over those of the pure HAp and the decrease in the case of the B-type model just because the nitrate ion is larger than OH^- but smaller than PO_4^{3-}. Such a trend is indeed observed in our calculations. The volume of the A-type supercell was found to increase by about 2% over the pure HAp supercell, whereas for the B-type configuration nearly no change in the cell volume was observed. However, the performed XRD measurements were not expected to reproduce the predicted trend because of the small concentration of the impurity.

To compare the propensities of NO_3^- incorporation in the different sites of HAp structure, we calculated the defect formation energies according to the following expressions:

$$E_{form}(A\text{-}NO_3) = E(A\text{-}NO_3) - E(bulk) - \mu_N - 2\mu_O$$
$$+ \mu_H \quad (2)$$

$$E_{form}(B\text{-}NO_3) = E(B\text{-}NO_3) - E(bulk) - \mu_N + \mu_{Ca} + \mu_P$$
$$+ \mu_O \quad (3)$$

where $E(bulk)$, $E(A\text{-}NO_3)$, and $E(B\text{-}NO_3)$ denote the total energies of the stoichiometric HAp cell and the HAp containing NO_3 defect in the A- or B-type configuration, respectively. μ_N is the chemical potential for the N atom. The chemical potentials for Ca (μ_{Ca}), P (μ_P), O (μ_O), and H (μ_H) are constrained by the thermodynamic equilibrium condition:

$$10\mu_{Ca} + 6\mu_P + 26\mu_O + 2\mu_H = \mu_{HAp} \quad (4)$$

and depend, in general, on the experimental preparation conditions. The value of μ_{HAp}, the chemical potential of HAp compound, at zero temperature (T = 0 K) and pressure equals that of $E(bulk)$.

As discussed in ref 47, in principle, the atomic chemical potentials have to be specified with respect to the corresponding reservoir phases. Thus, there is always some uncertainty in the determination of their values. In practice, one simply can construct the set of chemical potentials using the appropriate reference system. In the present work we consider two references. The first is chosen to be a set of an oxygen molecule (O_2), a hydrogen molecule (H_2), and bulk calcium (Ca_{bulk}). The second reference system comprises O_2, H_2, and a phosphorus pentoxide (P_2O_5) solid. The first reference system describes Ca-rich (equivalently, P-poor) preparation conditions, whereas the second one is related to P-rich (Ca-poor) case. With respect to the chemical potentials for O and H atoms, both of the reference systems correspond to O-, H-rich preparation limit, which we consider to be experimentally relevant. Of course, it is not a unique way to specify the chemical potentials, but we suggest that our description is adequate for the qualitative comparison of the stabilities of the studied structures depending on the preparation conditions.

With the determined above reference systems, using the total energies of the corresponding reservoir phases and eq 4 (the value of μ_N throughout the present work is derived from the total energy of N_2 molecule), the formation energies as obtained for 1 × 1 × 1 monoclinic supercell were calculated. The results are presented in Table 2. The computed values of E_{form} suggest that NO_3^- ion occupies preferentially the PO_4 site within a wide range of experimental conditions.

Table 2. Formation Energies E_{form} of NO_3^- Defects (in eV)

configuration	Ca-rich	P-rich
type A	0.39	0.39
type B	−7.26	−1.34

In order to study the structure and magnetic properties of the paramagnetic NO_3^{2-} center, we have performed spin-polarized GGA-PBE calculations by adding an extra electron. The structural relaxation was carried out with respect to atomic positions with the lattice parameters fixed. The optimized supercells containing the NO_3^- impurity were used as initial data. The structure of the resulting NO_3^{2-} radical shows significant deviation from the planarity for both A and B sites toward to the pyramidal shape (close to the C_{3v} symmetry). The out of plane deviation is estimated to be 13−14°. The value of the N−O bond length of NO_3^{2-} increases to 0.134 nm. The last value is slightly larger than predicted in refs 45 and 46.

Following Walsh[45] and Atkins and Symons[46] one expects the resulting NO_3^{2-} to be pyramidal with the C_{3v} symmetry, since in this case the extra electron is thereby stabilized: the 25th unpaired electron upon entering the antibonding $2a_2$ orbital causes bending of the 24-electron planar structure of the nitrate anion NO_3^-. The distortion introduces some s character to this orbital, reducing its antibonding, and both isotropic and anisotropic hyperfine contributions from the central N atom are expected to lead to the large values of the **A**-tensor components and their anisotropy in comparison to other radicals. The out of plane deviation was estimated to be in the range 10−16°. The NO bond lengths of the Y-shaped nitrate radicals are estimated to be 0.124 nm for NO_3 and up to 0.127 nm for NO_3^{2-}. No deviations from the axial symmetry were observed even in single crystals by X-band EPR.[48]

With the excellent stability of NO_3^{2-}, it could be expected that pyramidal symmetry of the radical fits tetrahedral B-sites rather than A-sites with axial symmetry. Calculations show that in both cases the unpaired electron is shared between the N and three O nuclei of the NO_3^{2-} radical (Figure 6). The values of spin density localization on N nucleus are calculated to be

0.29 e/bohr^3 for type A and 0.37 e/bohr^3 for type B substitutions, respectively.
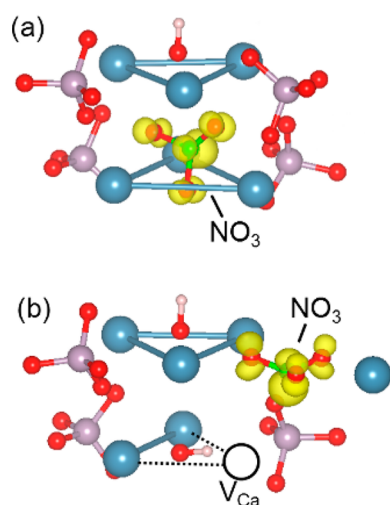

Figure 6. Optimized atomic structures of the most energetically favorable NO_3^{2-} defect complexes in (a) OH site (A-site) and (b) PO_4 site (B-site). V_{Ca} in (b) denotes the position of Ca vacancy. The isosurfaces for the spin density distribution (on the level of 0.01 e/bohr^3) are shown in yellow (Ca = blue, P = purple, O = red, H = white, N = green).

The principal values of hyperfine and **g** tensors as calculated using the GIPAW approach are presented in Table 3. The corresponding simulated pulsed EPR spectra (with a small noncoincidence of the directions of the principal axes of **A** and **g** taken into account) are plotted in Figure 2B in comparison with the experimental one. First of all, one can notice a dramatic difference between the components of the hyperfine tensor of A and B types of NO_3^{2-}. Moreover, the values obtained for the isolated NO_3^{2-} free radical (B3LYP/EPR-II; FR row in Table 3) have slightly better consistency with the experimental ones compared to those computed for the A-type substitution. This indicates that the coordinating environment significantly influences the magnetic properties of the NO_3^{2-} radical complex in the HAp lattice. From the excellent correspondence of the obtained spectroscopic parameters with the experimental results, it can be concluded that the observed NO_3^{2-} EPR spectrum originates from the B-site located radicals only. It is important to emphasize that the supercell size was found to have no significant influence on the calculated **A**-tensor.

In principle, when noticing closeness of the calculated spectroscopic parameters of the isolated NO_3^{2-} to the experimentally derived (Table 3) and high surface-to-volume ratio of nanosized samples, one might attribute the observed

EPR spectra to surface located paramagnetic centers. However, experimental evidence allows us to suggest definitely that the incorporated NO_3^{2-} radicals are obtained. The last conclusion is based on the detailed comparison of the noncarbonated nano- and micro-HAp (with the average crystallite sizes of 20–50 and 1000 nm, respectively) prepared by the similar wet procedure as used in the present work by exploiting high-frequency EPR and electron–nuclear double resonance (ENDOR) techniques.[49] No great difference between the observed EPR or ENDOR spectra of nitrate radicals in micro- and nanosamples as well as no great changes of those after the various chemical and annealing treatments of their surfaces were reported.

Sharp decrease of NO_3^{2-} concentration with the carbonation degree (Figure 4) in the range $0.5 < x < 1.0$ supports the conclusion about the nitrate location. Detailed experimental investigation of the microcrystalline carbonated HAp samples given in ref 31 shows that at $x < 0.25$ type A substitution is preferable. For $0.25 < x < 1.0$ type B and for $x > 1$, the redistribution between A and B sites is observed.

We note that performed DFT computation and experimental findings contradict the recent carbonate concerning DFT calculations[17] wherein it was concluded that the most energetically stable substitution for the carbonate ions is type A and then type B. It again emphasizes the importance of applying of the appropriate experimental analytical tools and methods for the comprehensive investigations of the HAp-based materials, as well as the importance of the healthy critical and even skeptical attitude to the huge amount of different types of numeric computing in materials sciences and biology which are not supported by experimental results.

From our experiments, at carbonate concentration of >7% the concentration of incorporated NO_3^{2-} is practically negligible (Figure 4). Therefore, we have provided one more piece of evidence that the carbonation process can "purify" the synthesized HAp based material, making the latter closer to the HAp of biogenic origin.

We have calculated the relative stability of the B-type CO_3^{2-} defect with respect to the B-type NO_3^-. For this the carbonate incorporation scheme in which the charge balance is maintained by the sodium ion $(Ca_{10-x}Na_x(PO_4)_{6-x}(OH)_2(CO_3)_x)$ was considered. We suggest that the use of only one of the possible configurations of CO_3^{2-} defect is sufficient for the first approach. It gives

$$\Delta E = E(B\text{-}CO_3) - E(B\text{-}NO_3) + \mu_N - \mu_C - \mu_{Na}$$
$$= -5.53 \text{ eV} \tag{5}$$

with the chemical potentials for Na (μ_{Na}) and C (μ_C) atoms derived from the energy of bulk Na and the CO_2 molecule, respectively. $E(B\text{-}CO_3)$ and $E(B\text{-}NO_3)$ were obtained for the

Table 3. GIPAW DFT Calculated Principal Components of ^{14}N Hyperfine Tensor A and g-Tensor for the A and B Types of NO_3^{2-} Defect Compared to the Experimental Values[a]

	g_x	g_y	g_z	Θ_g, deg	A_x, mT	A_y, mT	A_z, mT	Θ_A, deg
A-type	2.0081	2.0077	2.0017	75.8	2.478	2.485	5.183	74.6
B-type	2.0054	2.0052	2.0021	9.4	3.273	3.277	6.413	2.1
FR[b]	2.0057	2.0057	2.0017		3.077	3.077	5.752	
exptl	2.0055(5)	2.0055(5)	2.0015(5)		3.35(40)	3.35(40)	6.65(40)	

[a]Θ_g and Θ_A are the tilt angles of g_z and A_z principal directions with respect to the crystallographic b-axis, respectively. [b]FR denotes an isolated NO_3^{2-} "free radical" with the spectroscopic parameters calculated using ORCA B3LYP/EPR-II.

same locations of CO_3^{2-} and NO_3^- in the supercell. This finding is consistent with our experimental results and proves that the carbonate incorporation in HAp structure is energetically more favorable than the formation of the nitrate defect.

4. CONCLUSION

High sensitivity of the modern commercially available EPR spectrometers along with the pulsed techniques applied could be fruitfully used for the structural and elemental analysis of the HAp based materials. The observed influences could be used for the control of the desired structure, content, and impurity levels in the synthesis as well as in fundamental research.

In the present work, some of the obtained results could be summarized as follows:

(1) The computations based on the GIPAW DFT method reproduce the spectroscopic parameters of the radiation induced radical NO_3^{2-} in HAp with a high degree of accuracy. It appears that the measuring of the ^{14}N hyperfine splitting could shed light on the location(s) (type A or B) of nitrates in the HAp structure;

(2) Both thermodynamic and GIPAW DFT calculations show that B-type substitution (PO_4 site) is the preferable one for NO_3^-/NO_3^{2-}.

(3) The experimentally obtained spectroscopic parameters of stable nitrate radicals for nano-HAp samples practically coincide with the calculated values of those located in "micro-HAp" volume (no surface effects were taken into consideration) at least for the samples with the size of the crystallites down to 30 nm.

(4) The effects of the nitrate interplaying with other anionic substituents could be tracked through the changes of its EPR spectrum, as is shown for the carbonate ions.

(5) Carbonation could serve as a tool for decreasing the amount of the (un)desirable nitrate impurities in nano-HAp.

■ AUTHOR INFORMATION

Corresponding Author
*E-mail: marat.gafurov@kpfu.ru. Phone: +7(843) 2926480.
Notes
The authors declare no competing financial interest.

■ REFERENCES

(1) Lafon, J. P.; Champion, E.; Bernache-Assollant, D. Processing of A B - T y p e   C a r b o n a t e d   H y d r o x y a p a t i t e $Ca_{10-x}(PO_4)_{6-x}(CO_3)_x(OH)_{2-x-2y}(CO_3)_y$ Ceramics with Controlled Composition. *J. Eur. Cer. Soc.* **2008**, *28*, 139−147.

(2) LeGeros, R. Z. Properties of Osteoconductive Biomaterials: Calcium Phosphates. *Clin. Orthop. Relat. Res.* **2002**, *395*, 81−98.

(3) Dorozhkin, S. V.; Epple, M. Biological and Medical Significance of Calcium Phosphates. *Angew. Chem., Int. Ed.* **2002**, *41*, 3130−3146.

(4) Zhou, H.; Lee, J. Nanoscale Hydroxyapatite Particles for Bone Tissue Engineering. *Acta Biomater.* **2011**, *7*, 2769−2781.

(5) Dorozhkin, S. V. Nanodimensional and Nanocrystalline Calcium Orthophosphates. *Am. J. Biomed. Eng.* **2012**, *2*, 48−97.

(6) Wang, Zh.; Tang, Zh.; Qing, F.; Hong, Y.; Zhang, X. Applications of Calcium Phosphate Nanoparticles in Porous Hard Tissue Engineering Scaffolds. *NANO* **2012**, *07*, 1230004.

(7) Loo, S. C. J.; Moore, T.; Banik, B.; Alexis, F. Biomedical Applications of Hydroxyapatite Nanoparticles. *Curr. Pharm. Biotechnol* **2010**, *11*, 333−342.

(8) Uskoković, V.; Uskoković, D. P. Nanosized Hydroxyapatite and Other Calcium Phosphates: Chemistry of Formation and Application as Drug and Gene Delivery Agents. *J. Biomed. Mater. Res., Part A* **2011**, *96B*, 152−91.

(9) Chu, S. H.; Feng, D. F.; Ma, Y. B.; Li, Z. Q. Hydroxyapatite Nanoparticles Inhibit the Growth of Human Glioma Cells in Vitro and in Vivo. *Int. J. Nanomed.* **2012**, *7*, 3659−3666.

(10) Ma, Qi-Y.; Traina, S. J.; Logan, T. J.; Ryan, J. A. In situ lead imobilization by apatite. *Environ. Sci. Technol.* **1993**, *27*, 1803−1810.

(11) Mizuno, N., Ed. *Modern Heterogeneous Oxidation Catalysis: Design, Reactions and Characterization*; Wiley-VCH: Weinheim, Germany, 2009.

(12) Rivera-Muñoz, E. M. Hydroxyapatite-Based Materials: Synthesis and Characterization. In *Biomedical Engineering: Frontiers and Challenges*; Fazel-Rezai, R., Ed.; InTech: Rijeka, Croatia, 2011; pp 75−98.

(13) Landi, E.; Celotti, G.; Logroscino, G.; Tampieri, A. Carbonated Hydroxyapatite as Bone Substitute. *J. Eur. Ceram. Soc.* **2003**, *23*, 2931−2937.

(14) Girija, E. K.; Kumar, G. S.; Thamizhavel, A. Zinc and Carbonate Co-Substituted Nano-Hydroxyapatite. *AIP Conf. Proc.* **2011**, *1349*, 315−316.

(15) Moreira, M. P.; Da Silva Aragão, V. T.; De Almeida Soares, G.; Dos Santos, E. A. Simultaneous Insertion of Mg^{2+}, Sr^{2+} and Mn^{2+} Ions into Hydroxyapatite Structure. *Key Eng. Mater.* **2012**, *493−494*, 20−26.

(16) Fattibene, P.; Callens, F. EPR Dosimetry with Tooth Enamel: A Review. *Appl. Radiat. Isot.* **2010**, *68*, 2033−2116.

(17) Ren, F.; Lu, X.; Leng, Y. Ab Initio Simulation on the Crystal Structure and Elastic Properties of Carbonated Apatite. *J. Mech. Behav. Biomed.* **2013**, *26*, 59−67.

(18) De Leeuw, N. H. Computer Simulations of Structures and Properties of the Biomaterial Hydroxyapatite. *J. Mater. Chem.* **2010**, *20*, 5376−5389.

(19) Yavkin, B. V.; Mamin, G. V.; Orlinskii, S. B.; Gafurov, M. R.; Salakhov, M. K.; Biktagirov, T. B.; Klimashina, E. S.; Putlayev, V. I.; Tretyakov, Y. D.; Silkin, N. I. Pb^{3+} Radiation Defects in Ca_9Pb-$(PO_4)_6(OH)_2$ Hydroxyapatite Nanoparticles Studied by High-Field (W-Band) EPR and ENDOR. *Phys. Chem. Chem. Phys.* **2012**, *14*, 2246−2249.

(20) Gafurov, M. R.; Yavkin, B. V.; Biktagirov, T. B.; Mamin, G. V.; Orlinskii, S. B.; Izotov, V. V.; Salakhov, M. K.; Klimashina, E. S.; Putlayev, V. I.; Abdulyanov, V. A.; Ignatjev, I. M.; Khairullin, R. N.; Zamochkin, A. V.; Chelyshev, Y. A. Atherosclerotic Plaque and Hydroxyapatite Nanostructures Studied by High-Frequency EPR. *Magn. Reson. Solids* **2013**, *15*, 13102.

(21) Jarcho, M.; Bolen, C. H.; Thomas, M. B.; Bobick, J.; Kay, J. F.; Doremus, R. H. Hydroxyapatite Synthesis and Characterization in Dense Polycrystalline Form. *J. Mater. Sci.* **1976**, *11*, 2027−2035.

(22) Eachus, R. S.; Symons, M. C. R. Unstable Intermediates. Part L. The NO_3^{2-} Impurity Centre in Irradiated Calcium Carbonate. *J. Chem. Soc. A* **1968**, 790−793.

(23) Peckauskas, R. A.; Pullman, I. Nitrate Radicals in Apatites. *J. Dent. Res.* **1975**, *54*, 1096−1107.

(24) Bannov, S. I.; Nevostruev, V. A. Formation and Properties of NO_3^{2-}, NO_3 and $ONOO$ Radicals in Nitrate-Containing Matrice. *Radiat. Phys. Chem.* **2003**, *68*, 917−924.

(25) Brik, A. B.; et al. Nitrogen-Containing Ion-Radicals in Biogenic and Synthetic Calcium Phosphates. *Mineral. Zh. (Ukraine)* **2006**, *28*, 20−31 (in Russian).

(26) Vorona, I. P.; Ishchenko, S. S.; Baran, N. P.; Rudko, V. V.; Zatovskii, I. V.; Gorodilova, N. A.; Povarchuk, V. Y. NO_3^{2-} Centres in Synthetic Hydroxyapatite. *Phys. Solid State* **2010**, *52*, 2364−2368.

(27) Baran, N. P.; Vorona, I. P.; Ishchenko, S. S.; Nosenko, V. V.; Zatovskii, I. V.; Gorodilova, N. A.; Povarchuk, V. Y. NO_3^{2-} and CO_2^-

Centers in Synthetic Hydroxyapatite: Features of the Formation Under γ- and UV-irradiations. *Phys. Solid. State* **2011**, *53*, 1891−1894.

(28) Hukkanen, M. V. J.; Polak, J. M.; Hughes, S. P. F. *Nitric Oxide in Bone and Joint Disease*; Cambridge University Press: Cambridge, U.K., 1998.

(29) Islam, M.; Mishra, P. C.; Patel, R. Physicochemical Characterization of Hydroxyapatite and Its Application towards Removal of Nitrate from Water. *J. Environ. Manage.* **2010**, *91*, 1883−1891.

(30) Markovic, M.; Fowler, B. O.; Tung, M. S. Preparation and Comprehensive Characterization of a Calcium Hydroxyapatite Reference Material. *J. Res. Natl. Inst. Stand. Technol.* **2004**, *109*, 553−568.

(31) Kovaleva, E. S.; Shabanov, M. P.; Putlayev, V. I.; Filippov, Y. Y.; Tretyakov, Y. D.; Ivanov, V. K. Carbonated Hydroxyapatite Nanopowders for Preparation of Bioresorbable Materials. *Materialwiss. Werkstofftech.* **2008**, *39*, 822−829.

(32) De Keijser, T.; Langford, J. I.; Mittemeijer, E. J.; Vogels, A. B. P. Use of the Voigt Function in a Single-Line Method for the Analysis of X-ray Diffraction Line Broadening. *J. Appl. Crystallogr.* **1982**, *15*, 308−314.

(33) Giannozzi, P.; et al. QUANTUM ESPRESSO: A Modular and Open-Source Software Project for Quantum Simulations of Materials. *J. Phys.: Condens. Matter* **2009**, *21*, 395502.

(34) Perdew, J. P.; Burke, K.; Ernzerhof, M. Generalized Gradient Approximation Made Simple. *Phys. Rev. Lett.* **1996**, *77*, 3865−3868.

(35) Vanderbilt, D. Soft Self-Consistent Pseudopotentials in a Generalized Eigenvalue Formalism. *Phys. Rev. B* **1990**, *41*, 7892−7895.

(36) Yashima, M.; Yonehara, Y.; Fujimori, H. Experimental Visualization of Chemical Bonding and Structural Disorder in Hydroxyapatite through Charge and Nuclear-Density Analysis. *J. Phys. Chem. C* **2011**, *115*, 25077−25087.

(37) Monkhorst, H. J.; Pack, J. D. Special Points for Brillouin-Zone Integrations. *Phys. Rev. B* **1976**, *13*, 5188−5192.

(38) Pickard, C. J.; Mauri, F. All-Electron Magnetic Response with Pseudopotentials: NMR Chemical Shifts. *Phys. Rev. B* **2001**, *63*, 245101.

(39) Troullier, N.; Martins, J. L. Efficient Pseudopotentials for Plane-Wave Calculations. *Phys. Rev. B* **1991**, *43*, 1993−2006.

(40) Stoll, S.; Schweiger, A. EasySpin, a Comprehensive Software Package for Spectral Simulation and Analysis in EPR. *J. Magn. Reson.* **2006**, *178*, 42−55.

(41) Neese, F. ORCA Program System. *Wiley Interdiscip. Rev. Comput. Mol. Sci.* **2012**, *2*, 73−78.

(42) Palard, M.; Champion, E.; Foucaud, S. Synthesis of Silicated Hydroxyapatite $Ca_{10}(PO_4)_{6-x}(SiO_4)_x(OH)_{2+x}$. *J. Solid State Chem.* **2008**, *181*, 1950−1960.

(43) Abdul'yanov, V. A.; Galiullina, L. F.; Galyavich, A. S.; Izotov, V. G.; Mamin, G. V.; Orlinskii, S. B.; Rodionov, A. A.; Salakhov, M. K.; Silkin, N. I.; Sitdikova, L. M.; Khairullin, R. N.; Chelyshev, Y. A. Stationary and High-Frequency Pulsed Electron Paramagnetic Resonance of a Calcified Atherosclerotic Plaque. *JETP Lett.* **2008**, *88*, 69−73.

(44) Astala, R.; Stott, M. J. First Principles Investigation of Mineral Component of Bone: CO_3 Substitutions in Hydroxyapatite. *Chem. Mater.* **2005**, *17*, 4125−4133.

(45) Walsh, D. The Electronic Orbitals, Shapes, and Spectra of Polyatomic Molecules. Part V. Tetratomic Non-Hydride Molecules, AB3. *J. Chem. Soc.* **1953**, 2301−2306.

(46) Atkins, P. W.; Symons, M. C. R. *The Structure of Inorganic Radicals*; Elsevier: Amsterdam, 1967.

(47) Van de Walle, C. G.; Neugebauer, J. First-Principles Calculations for Defects and Impurities: Applications to III-Nitrides. *J. Appl. Phys.* **2004**, *95*, 3851−3879.

(48) Canniere, P. I.; Debuyst, R.; Dejehet, F.; Apers, D. ESR Study of Internally α-Irradiated (^{210}Po Nitrate Doped) Calcite Single Crystal. *Nucl. Tracks Radiat. Meas.* **1998**, *14*, 267−273.

(49) Gafurov, M.; Biktagirov, T.; Yavkin, B.; Mamin, G.; Filippov, Ya.; Klimashina, E.; Putlayev, V.; Orlinskii, S. Nitrogen-Containing Species in the Structure of the Synthesized Hydroxyapatite. *JETP Lett.*, accepted.